Machine Learning-assisted Optimization of a Single-atom Coordination Environment for Accelerated Fenton Catalysis

Haoyang Fu[a,b], Ke Li[c] , Chenfei Zhang[a], Jianghong Zhang[b], Jiyuan Liu[b], Xi Chen[b], Guoliang Chen[d], Yongyang Sun[b], Shuzhou Li[b*], Lan Ling[a*]

[a] State Key Laboratory for Pollution Control and Resource Reuse, College of Environmental Science and Engineering, Tongji University, Shanghai, 200092, China

[b] School of Materials Science and Engineering, Nanyang Technological University, 50 Nanyang Avenue, Singapore, 639798, Singapore

[c] Institute of Materials Research and Engineering, Agency for Science, Technology and Research, 138634, Singapore

[d] School of Energy Science and Engineering, Harbin Institute of Technology, Harbin 150001, China

Abstract

Machine learning (ML) algorithms will be the enablers in revolutionizing traditional methods of materials optimization. Here, we broaden the use of ML to assist the construction of Fenton-like single-atom catalysts (SACs) by developing a methodology including model building, train, and prediction. Our approach can efficiently extract synthesis parameters that exert a substantial influence on Fenton activity, and accurately predict the phenol degradation rate k of SACs with a mean error of ± 0.018 min^{-1}. The extended synthesis window with accelerated learning enables the realization that the heating temperatures during SACs synthesis significantly influence the Fe-N coordination number which ultimately dictates their performance. Through ML-guided optimization, a highly efficient SAC dominated by Fe-N_5 sites with exceptional Fenton activity (k = 0.158 min^{-1}) is identified. Our work provides an example for ML-assisted optimization of single-atom coordination environments and illuminates the feasibility of ML in accelerating the development of high-performance catalysts.

KEYWORDS

Machine Learning, Single-atom catalysts, Optimization, Fenton activity, Pollution control.

Graphical Abstract

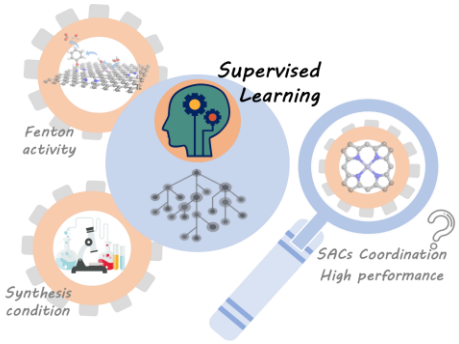

This study extends the ML method to optimize single-atom coordination environments. The application of the ML approach enables the rapid extraction of synthetic parameters affecting the coordination environments of SACs that determines the Fenton performance. Through ML-guided optimization, a SAC dominated by Fe-N_5 catalytic sites with exceptional Fenton activity in the SACs/H_2O_2 system was developed.

The discovery of single-atom catalysts (SACs) offers opportunities in catalysis by bridging the gap between heterogeneous and homogeneous catalysis [1-3]. The mononuclear nature of single-atom sites allows SACs to exhibit the highest utilization of the active centers and provide the opportunities to fine-tune controllably catalytic activity [4, 5]. Generally incorporating a transition metal single atom anchored to the support with the coordination of N/C atoms, and the resulting local coordination environment (M-N-C; M refers to the transition metal) is demonstrated to determine the catalyst activity [6-8]. Most of the reported SACs have been constructed by "bottom-up" strategy involving pyrolysis of the mixtures containing small-molecule metal precursors and N/C sources [5, 9-11]. However, numerous variables during SACs synthesis such as support composition, pyrolysis temperature, heating rate, etc., significantly exacerbate the unpredictability of M-N-C configuration, making it tough to unravel the accurate structure-efficiency relationships. Furthermore, exploration of high-performance SACs with optimized synthesis conditions is required to systematically consider the correlation of synthesis parameters, which is traditionally driven by an incremental trial-and-error method of learning. This often leads to slow experimental feedback that in turn impedes the progress of researchers who depend on timely results [12]. Therefore, an effective learning strategy towards optimizing construction of high-performance SACs is urgently desired.

As computational materials science nourishes, full-scale materials libraries, powered by machine learning (ML), can be built in less time than traditional experimental methods, which is becoming the workhorse for accelerating materials design [13-18]. As a robust computationally calculated tool, ML is commonly applied for prediction of material properties such as thermal conductivity [19-22], bulk and shear moduli [23-25], grain boundary energies [26], and crystal structures [27, 28]. While the design of high-performance materials through screening material synthesis parameters, which is the critical step for commercialization of materials, has not been widely

explored. In one pioneering study, Xu et al. implemented the ML model to optimize the chemical vapor deposition synthesis parameters, enabling the controllable growth of few-layered 1T'WTe_2 [29]. Such a data-driven synthesis approach would be the game-changer for rapid access to cost-effective materials in optimized performance. Nevertheless, direct prediction of performance from synthesis conditions inevitably affects the generality and scalability of the learning approach as each system is able to find an individual set of synthesis parameters to obtain the best performance, which leads to insufficient elaboration to capture subtle geometric dissimilarities [30]. For this, the crucial step for unraveling the synthesis complexity of SACs needs to build an understanding of how synthesis parameters influence the microenvironment, and then convert the data into an in-depth comprehension of the structure-efficiency relationship. Essential in ML algorithmic search is the requirement to balance between synthesis conditions, structural configuration, and catalysis performance.

In this work, the ML strategy is applied to speed up the design of high-performance Fenton-like SACs. As a typical iron-catalyzed advanced oxidation process (AOP), the Fenton/Fenton-like technology enables the effective generation of hydroxyl radicals (•OH, one of ROSs) by actuating the disproportionation of hydrogen peroxide (H_2O_2), which can indiscriminately transform organic molecules into harmless substances (e.g., CO_2, H_2O) to achieve pollutants degradation [31-33]. Through this accelerated platform, the SAC with outstanding degradation performance of phenol (a refractory organic pollutant; k= 0.158 min^{-1}) dominated by Fe-N_5 sites is identified, and the key interpretable descriptors during the synthesis process, namely calcination and pyrolysis temperatures, are determined to decode the correlation between the coordination structure and Fenton activity of SACs. As a proof-of-concept demonstration, typical SACs with different Fe-N coordination numbers (ranging from 2 to 5) are selected for the investigation of the correlation between catalytic activity and SACs fine structure. This study reveals the great promise of machine

learning to assist optimization of SACs coordination environment and accelerate design of other environmental materials.

Results/Discussion

The construction of SACs in this study is divided into two stages involving the synthesis of N-doped reduced graphene oxide support and the anchoring of Fe single atoms. The detailed synthesis process of SACs is shown in Figure S1. As a common ML procedure, an input dataset of SACs, each of which is described by descriptors, is constructed for training and testing ML model. Empirically, four experimental parameters related to the support synthesis process (i.e., N addition, calcination temperature, calcination time, and calcination heating rate) and four parameters related to the single-atom anchoring process (i.e., Fe addition, pyrolysis temperature, pyrolysis time, and pyrolysis heating rate) are screened as significant input descriptors. After that, a relatively small dataset is built by conducting 144 experiments in the laboratory with different combinations of synthesis parameters, collecting 1152 input data points and recording respective phenol degradation rate k (output variable) ranging from 0.01 to 0.15 min^{-1}. Tables S1 and Figure S2 provide a summary of the descriptors and initial datasets, respectively, showing that most variables are well-distributed within the selected range of values and suitable for the modeling. In ML applications, it is desirable to use descriptors with minimal redundant information, as they offer a more concise representation of the data, leading to increased efficiency and accuracy in the resulting models. Pearson's correlation coefficients are computed to measure the mutual information shared among all pairs of descriptors, providing a quantitative assessment of their interdependence. Figure 1a shows a scatter plot matrix of the selected descriptors employed in the ML model, revealing low linear correlations among them. This observation confirms the effectiveness of the descriptor selection process for training the ML model. To improve the

estimation of k from the descriptors, multiple regression models suitable for small datasets, including KNN, XGBoost, AdaBoost, and LASSO, are assessed utilizing the 10-fold cross-validation technique (Figure S3). The reasons why these four models are appropriate for training on the small dataset are described in the Supporting Information Note 2. Four prevalent performance metrics are employed to evaluate the ML models: R^2, MSE, MAE, and r. A comprehensive comparison and summary of the evaluation outcomes are presented in Figure 1b. It is noted that XGBoost model has the highest R^2 (0.87) and r (0.94) among the four trained model, which indicated that it can explain a larger proportion of the variance and has a stronger linear relationship with the dependent variable than the other models. Additionally, the lowest MAE (0.010) and MSE (0.014) for XGBoost model can also be found, revealing that the predicted k value is the closest to the actual values among the four models. The parity plot comparing experimentally measured k against predictions from the XGBoost ML model for training and testing dataset as shown in Figure S4. These metrics all suggest that the XGBoost model outperforms the other three models. In this regard, the XGBoost is selected as the ML model for further analysis.

Considering the optimization input ranges for each descriptor, the Fenton activities of the 269,080,000 resulting combinations have been estimated accordingly. Ten set of synthesis parameters with the highest predicted k values are selected for experimental verification, and the optimal descriptors and obtained results are shown in Table S2. The ML model predicts that adding 4 wt.% of Fe addition during synthesis results in SACs showing outstanding Fenton activity. Additionally, SACs synthesized at a calcination temperature between 640 and 680 °C and a pyrolysis temperature between 200 and 240 °C will exhibit relatively higher k values ($k > 0.160\ min^{-1}$). The experimental results confirm the validity of ML model in guiding the selection

of the synthesis parameters to optimize the Fenton activity of SACs, as shown that the average e r r o r

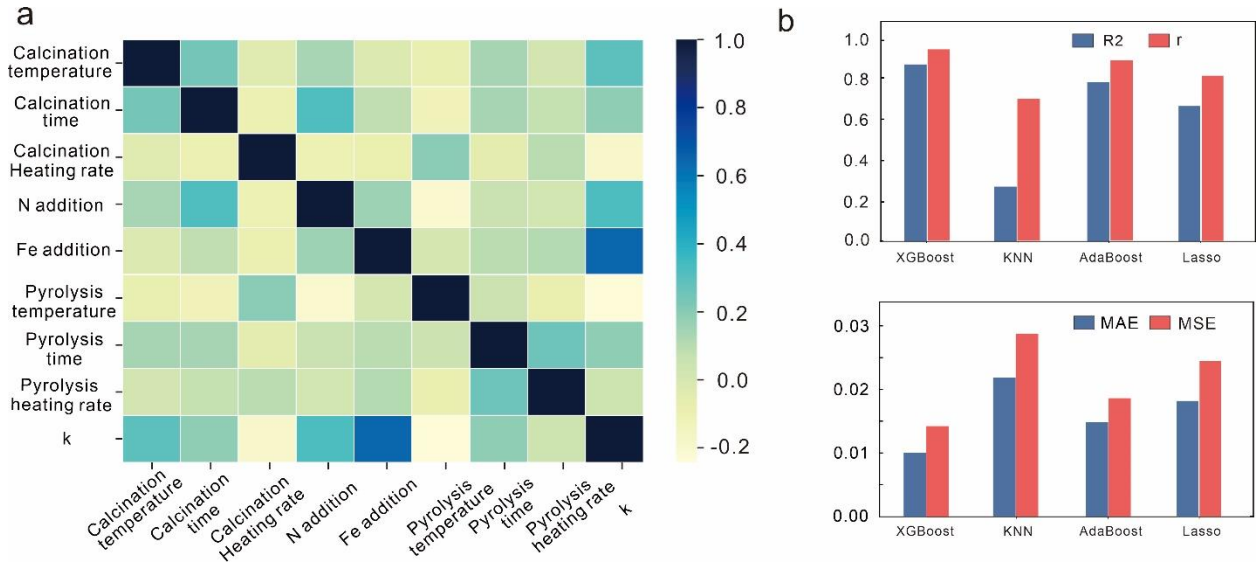

Figure 1. (a) The heat map of the Pearson's correlation coefficient matrix among the descriptors and degradation rate (k) of Fenton-like catalyst; (b) Barplot of the four candidate models' coefficient of determination (R^2), r (Pearson's correlation coefficient), mean absolute error (MAE) and mean squared error (MSE) indicating XGBoost-R is the best model.

between the predicted and experimental k value for all SACs is ± 0.018 min^{-1}, with a relative error of less than 12% (Table S2). The maximum phenol degradation rate in SACs reach 0.158 min^{-1} when the synthesis conditions are the Fe addition of 4 wt.%, the calcination time of 3 h, the calcination heating rate of 0.6 °C/min, the calcination temperature of 680 °C, N addition of 18%, Fe addition of 4%, the pyrolysis heating rate of 0.7 °C/min, the pyrolysis time of 2 h, and the pyrolysis temperature of 240 °C, which substantially surpasses the highest k in the original dataset. More importantly, such a high k value of ML-guided SAC is higher than most other reported state-of-the-art Fe-based Fenton-like catalysts (Figure 2a and Table S3) [34-42], which verifies the effectiveness of the trained ML model.

In order to gain a more comprehensive quantitative understanding of the catalytst synthesis system and unravel the complex relationships between descriptors and output presented in the

XGBoost-R model, we employed SHapley Additive exPlanations (SHAP) to elucidate the impact of these descriptors on the model's k value. SHAP provides a unified approach for interpreting machine learning models by utilizing additive feature importance measures, which have been demonstrated to be consistent with human intuition [43]. Figure 2b presents the evaluation of eight descriptors using their respective SHAP values. The feature ranking displayed on the y-axis signifies the importance of each descriptor within the predictive model. The SHAP value, represented on the x-axis, serves as a unified metric that quantifies the influence of a particular descriptor within the model. Each row features a violin plot that illustrates the attributions of descriptors to the model's outcome. The red portion of the violin plot denotes high feature values, while the blue portion corresponds to low feature values (Figure 2b left). The mean SHAP values are drawn with a histogram plot (Figure 2b right). As indicated, the Fe addition has the highest critical role in influencing the k value, followed by calcination and pyrolysis temperatures. Here the predicted results are represented by a 3D matrix constituted by the three most influential descriptors (i.e., Fe addition, calcination temperature, and pyrolysis temperature) to better interpret the key descriptors on phenol degradation (Figure 2c). The darkness of an area in the 3D matrix represents the level of Fenton activity, with darker areas indicating higher Fenton activity. It appears that the predicted k value increases with an increase in Fe addition and reaches a plateau when metal addition is 4 wt.% regardless of the calcination and pyrolysis temperatures. Justification for increased k value when the Fe addition < 4 wt.% is that the more Fe being introduced into the SAC enhances the ROS production since Fe acts as the activation center of H_2O_2 during the reaction, while higher metal addition (> 4 wt.%) cause the formation of metal clusters, resulting in reduced Fe utilization (Figure S4) [44]. Meanwhile, we must emphasize that the Fenton activity is significantly affected by the structure of SACs that is closely related to the

operating temperature during SACs synthesis [45, 46]. As shown in Figure 2d, at relatively low calcination temperature (< 600 °C), the k value continuously decreases with increased pyrolysis

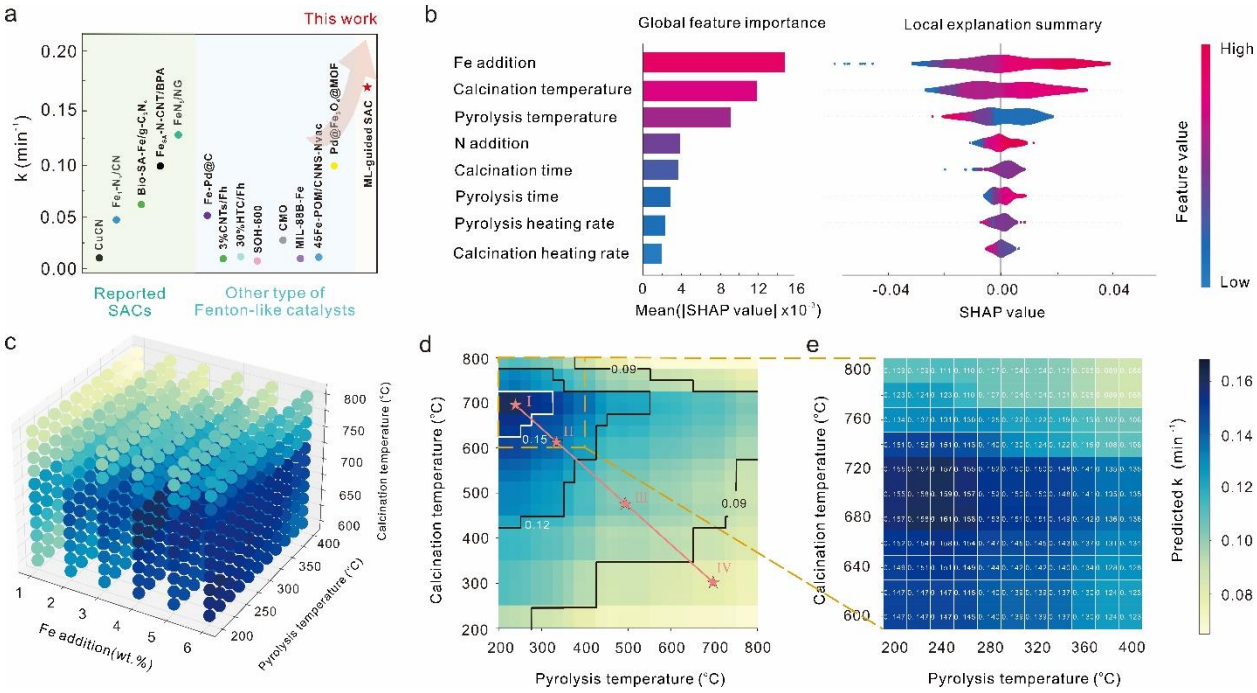

Figure 2. (a) Comparison of the polltant degradation kinetics by recently reported state-of-the-art Fe-based catalysts; (b) (left panel) Violin plot SHAP values for the XGBoost model. Red (blue) dots represent larger (smaller) values; (right panel) summary plot for SHAP analysis; (c) Predictions generated by the trained model are characterized by a 3D matrix, constituted by the three most influential descriptors; (d) Predictions (split into four different regions based on k values) derived from the trained model are depicted by a matrix that is composed of calcination and pyrolysis temperatures; (e) A amplification of the region with high k-values in (d)

temperature. For the higher calcination temperature (600-800 °C), the k value initially increases and then decreases (Figure 2e).

Inspired by the results that the microenvironment of SACs determines the Fenton activity, the behavior observed in the K-function of pyrolysis and calcination temperature is decoded. Along this way, four sets of synthesis parameters were selected to synthesize the catalysts according to the predicted k values in different regions of Figure 2d. The partitioning in Figure 2d here used the predicted k value as a basis. The obtained catalysts are named OSAC-I, OSAC-II, OSAC-III, and OSAC-IV, respectively, with detailed synthesis conditions described in Table S4. XRD patterns

of each SAC exhibit two typical peaks of graphic carbon with 2θ of about 25.6° and 43.2° (Figure S5). Raman spectra of four SACs in Figure S6 shows the D- and G-band peaks at ~1350 and 1590 cm^{-1}, respectively. Among the four SACs, OSAC-IV has the lowest intensity ratio of the D-band to the G-band (I_D/I_G= 0.90), indicating the highest extent of graphitization. HAADF-STEM reveals the presence of multiple bright dots (marked with yellow circles) without obvious aggregation found on both SACs (Figure 3a), revealing the single-atom nature of Fe species. EDS mappings of all four SACs show a uniform distribution of the N, Fe, and C species (Figure 3b, Figure S7). Quantitative analysis of elemental content reveals that four Fe SACs have the similar Fe contents (~ 3 wt%) but different N contents (Table S5).

The SAC with less N content in support has a lower Fe oxidation state, as evidenced by the negative shift of binding energy from OSAC-I to OSAC-IV in the XPS spectra of Fe 2p3/2 region. The atom ratio of Fe^{2+} to Fe^{3+} species of OSAC-I, OSAC-II, OSAC-III, and OSAC-IV are evaluated as 0.89, 1.26, 1.43, and 2.14, respectively (Figure S8). Additionally, a gradual decrease of the pyridinic N content and an increase of graphitic N content from OSAC-I to OSAC-IV can be found in the N 1s spectrum. Noted that the deconvoluted peaks at 399.6 eV corresponding to Fe-N_x species for all SACs emerge compared with N-rGO (Figure 3c) [40], which demonstrates the coordination environment of Fe sites is associated with N species. In case the local coordination structure of heterogeneously anchored single atoms is often considered a rigid ligand that is embedded on the catalyst surface, the catalytic activity of SACs is supposed to be controlled predominantly by modulating this coordination environment. In this regard, the coordination environments of single-atom Fe on FeN_x are further investigated by Mössbauer spectroscopy characterization. As shown in Figure 4a, all the four SACs contain five doublet components labeled as D1, D2, D3, D4, and D5 sites. The D1 site represents the XY-FeN_x moieties (X, Y refer to two ligands such as O, N) featuring a medium spin state of the Fe center [47, 48]. The isomer shift

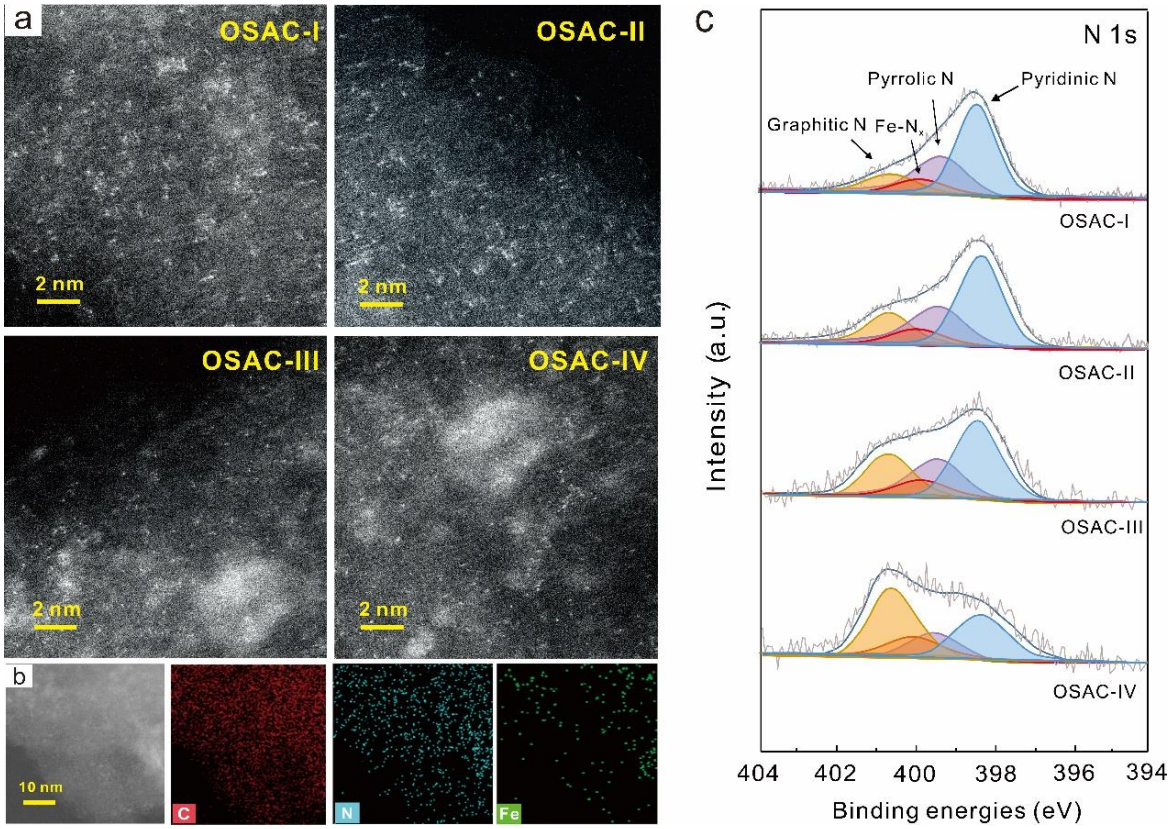

Figure 3. (a) HAADF-STEM images of the OSAC-I, OSAC-II OSAC-III, and OSAC-IV; (b) EDS mapping (C, N, and Fe) of OSAC-I; (c) N 1s XPS of the OSAC-I, OSAC-II OSAC-III, OSAC-IV.

(IS) and quadrupole splitting (QS) values for D2 site are about 0.4 mm/s and 2.6 mm/s, respectively, which is typically deemed as the low-spin Fe(II)N_4 architecture (Table S6) [49]. The doublets D3, which featured the largest IS value (0.43-0.47 mm/s) among the five doublets, are assigned to N–Fe(II)N_4 species with a penta-coordinated structure [50, 51]. The larger IS for the N–Fe(II)N_4 species compared to Fe(II) in a four-coordinated structure can be ascribed to the existence of more N atoms around the Fe ion, which enables a more delocalized 3d electron density around the Fe center. This results in a stronger electrostatic interaction between the Fe center and the surrounding electrons, leading to a larger shift in energy [52]. Thus, the D4 and D5 sites with a smaller IS value than that of Fe(II)N_4 can be assigned to two Fe(II)$N_{a/b}$-like species with Fe-N coordination number less than 4, while D5 has a lower coordination number than D4 [47, 53]. The

relative amounts of different Fe species on each SAC are measured by calculating spectral area. It can be found that all SACs contain a large amount of XY-FeN_x moieties, which may arise from the sorption of air molecules on the FeN_x sites [47, 48]. Additionally, the content of Fe species labeled D3, D2, D4, D5 make up a significant portion in OSAC-I (34.1%), OSAC-II (37.8%), OSAC-III (20.5%), and OSAC-IV (24.6%), respectively (Table S6), implying that the OSAC-I has the highest Fe-N average coordination number among four SACs, and follows the order OSAC-I > OSAC-II > OSAC-III > OSAC-IV.

To further analyze the coordination structure of SACs, XAS characterization was performed and the results are shown in Figure 4b. Fe K-edge X-ray absorption near-edge structure (XANES) spectra show that the energy absorption threshold of each SAC locates between FePc and Fe_2O_3, indicating the average Fe valence is between +2 and +3. The pre-edge centroid shifts slightly to lower energy from OSAC-I to OSAC-IV, suggesting the decreased average Fe oxidation state, which is in accordance with the XPS results. The Fourier transformed (FT) spectra of Fe K-edge extended X-ray absorption fine structure (EXAFS) of all four SACs show a scattering path located at about 1.44 Å, which is assigned to the Fe-N/O bond (Figure 4c) [54]. The EXAFS wavelet transforms (WT) plot of all SACs observe a WT maximum at 3.7 $Å^{-1}$, which can be identified as the Fe−N bonding by comparing with related references (i.e., Fe_2O_3, Fe foil, and FePc) (Figure 4d). The insignificant backscattering of Fe at a distance of ~2.18 Å from Fe−Fe bonds suggests the sole existence of atomically dispersed Fe sites in all samples. The quantitative coordination of Fe atoms is obtained after EXAFS fitting (Figure S9, Table S7), revealing that the Fe-N coordination number of OSAC-I, OSAC-II, OSAC-III, and OSAC-IV are 5.2, 4.0, 3.2, and 1.9, while the Fe-C coordination numbers of OSAC-III and OSAC-IV are 0.8 and 1.8, respectively, which are in agreement with the optimized atomic structures as determined by DFT calculations. These result, combined with the above Mössbauer analysis, suggest that the Fe species in OSAC-

I, OSAC-II, OSAC-III, and OSAC-IV is predominantly Fe-N_5, Fe-N_4, Fe-N_3C, and Fe-N_2C_2 site, respectively. Figure S9 shows the dominant Fe coordination environment configurations for each SAC.

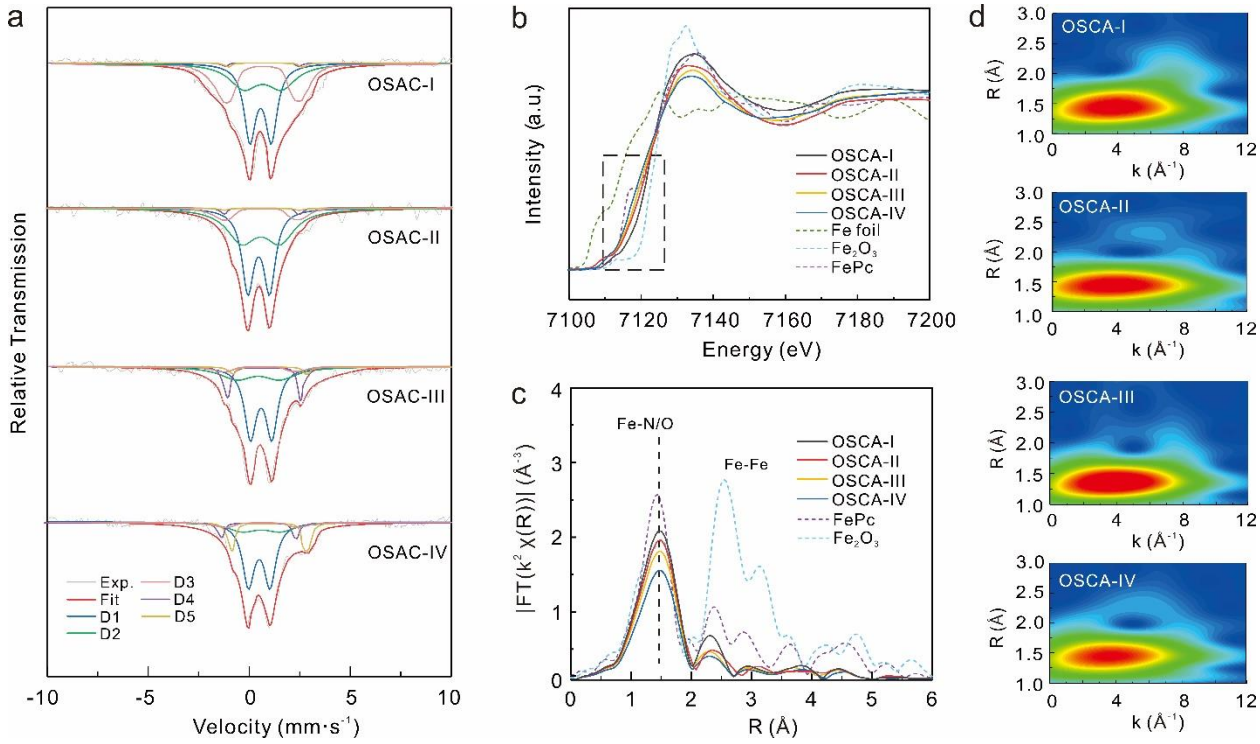

Figure 4. (a) ^{57}Fe Mössbauer spectra of OSAC-I, OSAC-II OSAC-III, and OSAC-IV; (b) Fe K-edge XANES spectra and (c) Fe K-edge FT-EXAFS of the OSAC-I, OSAC-II OSAC-III, OSAC-IV, Fe foil, FePc, and Fe_2O_3; (d) Fe K-edge WT-EXAFS of the OSAC-I, OSAC-II OSAC-III, and OSAC-IV.

We then seek how the microenvironment affects the Fenton performance to establish the correlation for catalytic activity and structure. Here, a systematical evaluation of the Fenton activity in the SACs/H_2O_2 systems is performed. The control experiments show the H_2O_2 cannot effectively degrade phenol and only ~ 1% phenol can be removed within 50 min (Figure 5a), which elucidates the limited contributions of H_2O_2 alone on the phenol removal. The significantly improved phenol removal efficiency once the introduction of SACs implied the effective H_2O_2 activation by Fe center of SACs. Among four SACs, the OSAC-I exhibits the highest Fenton activity with the k of 0.158 min^{-1}, followed by the OSAC-II/H_2O_2 (0.127 min^{-1}), OSAC-III/H_2O_2

(0.091 min^{-1}) and OSAC-IV/H_2O_2 systems (0.070 min^{-1}) (Figure S10). Such a high H_2O_2 activation ability for the OSAC-I/H_2O_2 system translates into the best total organic carbon (TOC) removal performance among four SACs (Figure S11). The recycling and leaching experiments show that OSAC-I still has a high degradation rate after 5 cycles (Figure S12) and almost no iron (< 0.2 mg/L) is leached during phenol degradation (Figure S13), indicating that OSAC-I has a high stability in the Fenton-like reaction. Depending on the specific activity and microenvironment of the SACs obtained above, the structure-performance correlations of structure parameters (i.e., the coordination number of Fe-N, BET surface area, the Fe oxidation state, or normalized Fe content) with Fenton activity are further analyzed. Figure 5b and Figure S14 show the relationship between structural parameters and k values. It is interesting to find that the oxidation state of Fe center is an almost linear negative correlation with the coordination number of Fe-N, which suggests the electronic structure is mainly influenced by the coordination of individual atoms with adjacent donor atoms, specifically N in this case. It is explainable that the electronic properties of the N atom point to its stronger ability than the C atom to attract electrons from electron-rich single-atom Fe, which results in the highest oxidation of the FeN_5-dominated OSAC-I and lowest oxidation of the FeN_2C_2-dominated OSAC-IV. It seems that the increased oxidation is not favorable for the Fenton/Fenton-like reaction due to the slowing down of the key chain reaction of Fe^{2+} and H_2O_2 (forming •OH responsible for the pollutants degradation). However, the catalytic activity in our case increases with increasing oxidation state of SACs, which implies that the oxidation state of Fe does not necessarily dominate H_2O_2 activation process. When further correlating the coordination number of Fe-N with the Fenton-like performance, we could get an approximately linear correlation between them, namely, the smaller coordination number of Fe-N, the lower Fenton activity (Figure 5b). The small deviation of k value from the fitted curve for OSAC-IV may be caused by other factors, such as the effect of oxidation state on the Fenton activity.

Comparatively, no obvious correlation between both BET surface area and normalized Fe content with the reaction rate constant can be found (Figure S14). These results reveal that the Fenton specific activity depends predominantly on the coordination number of Fe-N in the SACs.

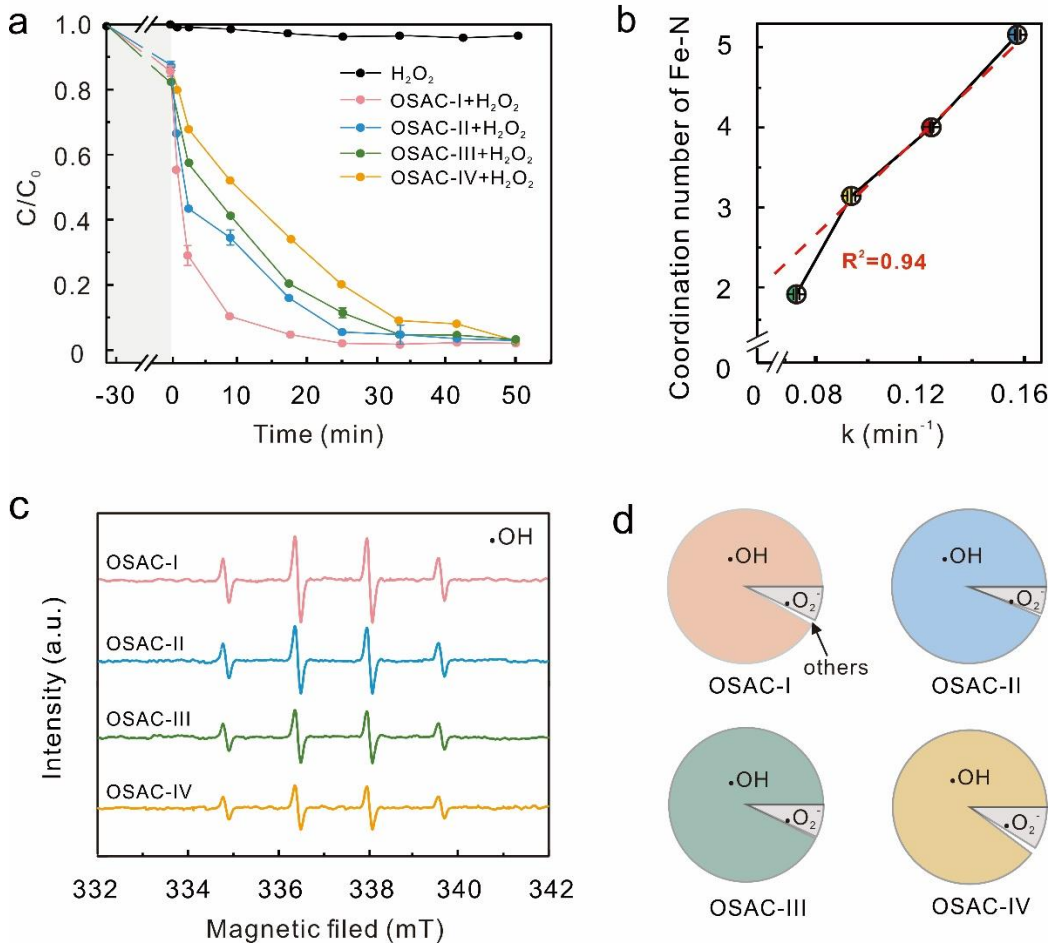

Figure 5. (a) Phenol degradation performance of OSAC-I, OSAC-II OSAC-III, and OSAC-IV (pH= 5.0 ± 0.2, [Catalyst]= 0.1 g/L, [phenol]= 20 mg/L, [H_2O_2] = 10 mmol/L); (b) The relationship between k and the coordination number of Fe-N; (c) ESR spectra for the detection of •OH in the existence of DMPO; (d) ROSs distribution during phenol degradation by OSAC-I, OSAC-II OSAC-III, and OSAC-IV.

To further understand the coordination structure-Fenton activity relationship, the ESR and free radical quenching experiments were conducted to identify ROS that contribute to phenol degradation. As shown in Figure 5c, the signal of DMPO-•OH with 4-fold characteristic peaks in an intensity ratio of 1:2:2:1 is observed in all four SACs/H_2O_2 systems, which indicates the

generation of •OH during phenol degradation. Additionally, the detection of DMSO−•O_2^- in DMSO dispersions can be found, suggesting that the •O_2^- is also involved during the Fenton-like reaction (Figure S15). Minor detection of the $^1O_2$ signal by TEMP spin trapping and the low concentration of PMSO2 detected exclude the possibility of nonradical ROS and Fe(IV) species as the dominant oxidants during phenol degradation (Figure S16, S17). The radical quenching experiments show that the degradation rate in the all SACs/H_2O_2 systems remains at a relatively high level after the introduction of BQ (•O_2^- scavenger), while the degradation rate has an obvious drop using IPA as the •OH scavenger (Figure S18). These results indicate a primary role of •OH for the phenol degradation during the Fenton-like reaction. The contributions of •OH, •O_2^-, and others are calculated using the method reported by Xu et al. [32] (See the section Method). The results show that •OH accounted for more than 90% of the contribution to phenol degradation in all four SACs/H_2O_2 systems (Figure 5d). Therefore, the strongest EPR signal of DMPO-•OH observed in Figure 5c in the OSAC-I/H_2O_2 system implies the highest generation efficiency of •OH among four systems, resulting in exhibiting the best Fenton activity. The effective generation of •OH for OSAC-I can be further evidenced by DFT calculations. The H_2O_2 activation pathway under the acidic catalytic milieu and the intermediates structures in FeN_5, FeN_4, FeN_3C, and FeN_2C_2 models are provided in Figure S19-23. The DFT adsorption energies, zero-point energies (ZPE), entropy (TS) and solvation corrections, ZPE-TS for substrate and adsorption intermediates needed to calculate free energies are available in Table S8-11. The energy diagram of the H_2O_2 activation process reveals that the dissociation of one OH* to produce a •OH is the rate-determining step (RDS) for all models, with a Gibbs free energy increase of 0.28, 0.74, 0.89, and 1.31 eV for the FeN_5, FeN_4, FeN_3C, and FeN_2C_2 models, respectively (Figure S24). A lower energy barrier for RDS implies a more favorable production of •OH, and the FeN_5 site has the lowest energy barrier of RDS, followed by FeN_4, FeN_3C, and FeN_2C_2. This indicates that the production of •OH

theoretically follows the FeN_5 > FeN_4 > FeN_3C > FeN_2C_2 site, which is consistent with the radical quenching experiments showing the generation efficiency of •OH follows a FeN_5 > FeN_4 > FeN_3C > FeN_2C_2 dominated SAC. Therefore, the key role of Fe-N coordination number for the generation of the reactive •OH is confirmed by the DFT calculations. The ML-guided SAC with predominantly FeN_5 site has the ability to effectively generate active •OH and thus exhibits the superior reaction kinetics rate that can be interpreted.

Conclusions

In conclusion, this study extends the ML approach to the construction of Fenton-like SACs. The application of the ML approach enables the rapid extraction of synthetic parameters affecting the Fenton activity of SACs and the accurate prediction of phenol degradation rates with low mean error (± 0.018 min^{-1}). The calcination temperature during support construction and the pyrolysis temperature during single atom anchoring significantly influences the Fe-N coordination number of the SAC are revealed, which ultimately dictating the catalytic performance of SACs. Through ML-guided optimization, a SAC dominated by Fe-N_5 catalytic sites was developed, which demonstrated exceptional Fenton activity with a k of 0.158 min^{-1} in the SACs/H_2O_2 system, which far exceeds than most other Fe-based Fenton-like catalyst. Overall, our work provides an example of understanding the synthesis-structure-property relationships of Fenton-like SACs with the aid of ML, which can effectively facilitate the SACs commercialization.

Methods/Experimental

Synthesis of SACs

Here engineered Fe element, the most commonly used metal in Fenton/Fenton-like systems, is used to activate H_2O_2.The SACs in our study were constructed applying a two-steps strategy, which consists of two steps: (1) synthesis of N-doped reduced graphene oxide support, and (2) anchoring of Fe single atoms. The detailed synthesis protocol is provided in Figure S1. Briefly, 3 mL of ammonia (28 wt%; Aladdin Industrial Co., China) and 200 μL of hydrazine hydrate (80 wt%; Aladdin Industrial Co., China) were hybrid with 400 mL of 1 g/L aqueous graphene oxide (GO) dispersed into a 1 L three-necked flask with continuous stirring for 15 min. The reduced graphene oxide (rGO) was obtained by heating as-synthesized mixture in an oil bath at 95 °C up to 60 min. After that, 0.11-0.43 g urea (CH_4N_2O, Aladdin Industrial Co., China) was mixed with 1 g of rGO into a 50 mL of deionized water (DI) for 30 min and subsequent freeze-drying. The resulting solid was transferred to a quartz boat and calcinated at 100-800 °C for 0-4 h at a ramp of 0.1-1 °C/min and then washed with DI to obtain N-rGO support. Next, the as-synthesized N-rGO was admixed with 0-40.8 mg of FePc (a typical metal precursor for Fe SACs synthesis) in 10 mL of DI and then pyrolyzed at 100-800 °C for 0-4 h at a heating rate of 0.1-1 °C/min. The remaining solid was washed with DI several times and then dried to get targeted SACs.

Analysis and characterization

The X-ray powder diffraction (XRD) patterns are taken with a Bruker D8 Advance X-ray diffractometer (Bruker AXS, German). The morphology and microstructure are measured with scanning/transmission electron microscopy (S/TEM) using Cs-corrected FEI TitanTM G2 60–300 instrument (FEI Ltd., Eindhoven, the Netherlands) operating at 300 kV, with energy dispersive X-ray spectroscopy (EDS) for catalyst composition analysis. Raman spectra are obtained by a

Renishaw inVia confocal Raman microscope (WITec Instruments Corp., Germany), equipped with a 50x objective, 1800 l/mm grating, and a 532 nm excitation laser. X-ray photoelectron spectroscopy (XPS) analyses of supports and catalysts are measured using ESCALAB 250Xi (Thermo Fisher Scientific, USA). The Mössbauer measurements are carried out using the Wissel MS-500 spectrometer (WissEI, Germany) in transmission geometry with constant acceleration mode. X-ray absorption structure (XAS) measurements are conducted at the X-ray Absorption Fine Structure for Catalysis beamline of Singapore Synchrotron Light Source center.

Examination of SACs

Batch experiments are carried out to assess the Fenton activities of produced SACs. The procedure involves adding 2.0 mg of the SACs to a 20 ml solution of phenol (20 mg/L) and allowing it to reach adsorption-desorption equilibrium after 30 min. 10 mmol/L of H_2O_2 aqueous solution is then added for the phenol degradation. The reaction pH is maintained at 5.0 using a buffer solution of acetic acid and sodium acetate (0.2 mmol/L). At certain time intervals, a 2-mL suspension is collected, filtered through 0.22 μm fibers, and then quenches by 0.2 mL of 0.2 mM of sodium hyposulfite solution to measure phenol concentration. Phenol concentration is quantified using the TU-1901 ultraviolet (UV)-visible (vis) spectrophotometer (Beijing Puxi Inc., China) with the absorbance at 280 nm. Electron spin resonance (ESR) measurements are performed using spin-trapping agents such as 5,5-Dimethyl-1-pyrrolidine-N-oxide (DMPO), dimethyl sulfoxide (DMSO), and 4-Amino-2,2,6,6-tetramethylpiperidine (TEMP). The PMSO and its oxidation product (phenyl methyl sulfone; $PMSO_2$) are detected using a high-performance liquid chromatography (HPLC, Alliance 2695, Waters, USA), equipped with an ACQUITY UPLC@BEH C18 column (2.1×50 mm, 1.7 μm, Waters, USA). Isopropanol (IPA; 2 mL) and p-benzoquinone (BQ; 15 mg) are chosen as scavenges of •OH and $•O_2^-$, respectively. The contributions of •OH, $•O_2^-$ and others during degradation are quantitively determined. The reaction

rate constants after adding IPA, BQ were denoted as k_1, k_2, respectively, and the initial rate constant without quenching agent was k_0. The contributions of •OH, $•O_2^-$ and others were calculated according to Eqs. 1-3:

$$\lambda(\bullet OH) = \left[\left(k_0 - k_1\right) / k_0\right] \times 100\% \quad (1)$$

$$\lambda\left(\bullet O_2^-\right) = \left[\left(k_0 - k_2\right) / k_0\right] \times 100\% \quad (2)$$

$$\lambda(\text{ others }) = 1 - \lambda(\bullet OH) - \lambda\left(\bullet O_2^-\right) \quad (3)$$

where λ(•OH), λ($•O_2^-$), and λ(others) are the contributions of •OH, $•O_2^-$ and others in the reaction process, respectively.

Data collection for machine learning

The process of data collection involves gathering a training set for the ML model, which includes eight descriptors (input) and one label (output). Specifically, the input descriptors of models consist of four SACs synthesis parameters related to the support synthesis process (i.e., N addition, calcination temperature, calcination time, and calcination heating rate) and four parameters related to the Fe single-atom anchoring process (i.e., Fe addition, pyrolysis temperature, pyrolysis time, and pyrolysis heating rate), which are empirically considered to be the essential parameters of pyrolysis-synthesized SACs by the experimentalists. The phenol degradation rate k of SACs is selected as the output variable. By synthesizing and evaluating the Fenton activity of 144 SACs, 144 datasets consisting of 1152 input data points and 144 output data points are collected for ML exploration. The data set is comprised of a wide range of calcination/pyrolysis temperatures ranging from 100 to 800 ° C, calcination/pyrolysis times from 0 to 4 h, calcination/pyrolysis heating rate from 0.1 to 1 °C/min, N addition from 5 to 20%, and Fe addition from 0 to 6%, respectively. The phenol degradation rate of obtained catalysts covers a wide range

of 0.01-0.15 min^{-1}. A detailed overview of the descriptors and their selected value ranges, as well as the histograms of the datasets for the descriptors are shown in Table S1 and Figure S2.

Machine learning algorithms and DFT computation methods

Based on the "no-free-lunch theorem", there is no single algorithm that is universally optimal for solving all problems. Consequently, when choosing an algorithm to solve a specific problem, it is crucial to consider the problem's particular characteristics and select an algorithm that is well-suited to those characteristics. In this work, representative ML models include Least absolute shrinkage and selection operator (LASSO), k-nearest neighbors (KNN), Adaptive Boosting (AdaBoost), and eXtreme Gradient Boosting (XGBoost) algorithms are considered to train. A detailed discussion of the characteristics of each model is provided in the Supporting Information Note 1. All models are constructed utilizing Python's scikit-learn library. Four optimal ML models from the LASSO, KNN, AdaBoost and XGBoost algorithms are obtained after training with 80% of the dataset and testing using the remaining 20% of the dataset. The hyperparameters for each algorithm are tuned to obtain the minimal mean-squared error for k value based on 10-fold cross-validation with varying hyperparameters. In LASSO, the λ parameter is the tuned hyperparameter to improve the performance of the model. In KNN, the number of nearest neighbors that controls the level of smoothing in the model is tuned. In AdaBoost, both the learning rate and the number of estimators, which are crucial hyperparameters governing the model's complexity, are optimized. For the XGBoost, several hyperparameters including the number of estimators, the number of features use in each tree, the maximum depth of each tree, the learning rate use to weight each model, and the number of samples used in each tree are tuned to improve the model convergence. The coefficient of determination (R^2), Pearson correlation coefficient (r), mean-absolute error (MAE) and mean square error (MSE) are utilized to compare the prediction accuracy and quantify

the prediction performance. The definition of the R^2, r, MAE, and MSE are provided in the Supporting Information Note 2.

The density functional theory (DFT) calculations of this study are all calculated by the Vienna Ab initio Simulation Package (VASP) program. The FeN_5 and three FeN_xC_{4-x} (x=1, 2, and 3) models are constructed by loading a single Fe atom on the 6×4×1 nitrogen-doped graphene. The adsorption energy E_{ad} of intermediates onto Fe-N-C sites are calculated to evaluate the H_2O_2 activation performance of the catalytic sites. The detailed computation methods can be found in the Supporting Information Note 3.

ASSOCIATED CONTENT

Supporting Information

The Supporting Information is available free of charge at xxx

Additional details including the description of ML models and DFT methods, scattering matrix of correlation for descriptors, schematic illustration for the synthesis of pyrolysis-based SACs, schematic of the model selection workflow, the kinetic plots for the phenol degradation of SACs, TOC degradation kinetic and PMSO2 production in the SACs+H_2O_2 systems, and additional supporting STEM, XRD, EDS, Raman, Mössbauer, EXAFS, ESR, DFT data

AUTHOR INFORMATION

Corresponding Authors

Lan Ling — State Key Laboratory for Pollution Control and Resource Reuse, College of Environmental Science and Engineering, Tongji University, Shanghai, 200092, China; orcid.org/0000-0001-7348-4657; Email: linglan@tongji.edu.cn

Shuzhou Li — School of Materials Science and Engineering, Nanyang Technological University, 50 Nanyang Avenue, Singapore, 639798, Singapore; orcid.org/0000-0002-2159-2602; Email: lisz@ntu.edu.sg

Authors

Haoyang Fu — State Key Laboratory for Pollution Control and Resource Reuse, College of Environmental Science and Engineering, Tongji University, Shanghai, 200092, China; orcid.org/0000-0001-8755-1144

Ke Li — Institute of Materials Research and Engineering, Agency for Science, Technology and Research, 138634, Singapore

Chenfei Zhang — State Key Laboratory for Pollution Control and Resource Reuse, College of Environmental Science and Engineering, Tongji University, Shanghai, 200092, China

Jianghong Zhang — School of Materials Science and Engineering, Nanyang Technological University, 50 Nanyang Avenue, Singapore, 639798, Singapore

Jiyuan Liu — School of Materials Science and Engineering, Nanyang Technological University, 50 Nanyang Avenue, Singapore, 639798, Singapore

Xi Chen — School of Materials Science and Engineering, Nanyang Technological University, 50 Nanyang Avenue, Singapore, 639798, Singapore

Guoliang Chen — School of Energy Science and Engineering, Harbin Institute of Technology, Harbin 150001, China

Yongyang Sun — School of Materials Science and Engineering, Nanyang Technological University, 50 Nanyang Avenue, Singapore, 639798, Singapore

Zibiao Li — Institute of Materials Research and Engineering, Agency for Science, Technology and Research, 138634, Singapore

Author Contributions

H. F. 'contributed' Conceptualization, Methodology, Software, Data curation, Writing – original draft preparation; **K. L.** and **C. Z.** 'contributed' Data curation, Writing – original draft preparation. **J. L., Z. L.,** and **J. Z.** 'contributed' Data curation, Investigation. **X. C., G. C.** and **Y.**

S. 'contributed' Visualization, Investigation. **L. L.** and **S. L.** 'contributed' Supervision, Conceptualization, Writing – review & editing.

Notes

The authors declare no competing financial interest

ACKNOWLEDGMENT

This work was supported by the grant from the National Science Fund for Excellent Young Scholars (No. 21822607), the National Natural Science Foundation of China (No. 22176147), Singapore Ministry of Education Tier 2 (No. MOE-T2EP10220-0005) and Tier 1 (RG8/20), China Scholarship Council (202106260199), the Fundamental Research Funds for Central Universities (No. 22120200178). The computational work for this article was fully performed on resources of the National Supercomputing Centre, Singapore (https://wwwnsc.sg).

REFERENCES

(1) Huo, M.; Wang, L.; Wang, Y.; Chen, Y.; Shi, J. Nanocatalytic tumor therapy by single-atom catalysts. *ACS Nano* **2019**, 13, 2643-2653.

(2) Han, L.; Cheng, H.; Liu, W.; Li, H.; Ou, P.; Lin, R.; Wang, H. T.; Pao, C. W.; Head, A. R.; Wang, C. H.; Tong, X.; Sun, C. J.; Pong, W. F.; Luo, J.; Zheng, J. C.; Xin, H. L., A single-atom library for guided monometallic and concentration-complex multimetallic designs. *Nat. Mater.* **2022**, 21, 681-688.

(3) Qiao, B.; Wang, A.; Yang, X.; Allard, L. F.; Jiang, Z.; Cui, Y.; Liu, J.; Li, J.; Zhang, T., Single-atom catalysis of CO oxidation using Pt_1/FeO_x. *Nat. Chem.* **2011**, 3 (8), 634-41.

(4) Gawande, M. B.; Fornasiero, P.; Zbořil, R., Carbon-based single-atom catalysts for advanced applications. *ACS Catal.* **2020**, 10 (3), 2231-2259.

(5) Zhou, X.; Ke, M. K.; Huang, G. X.; Chen, C.; Chen, W.; Liang, K.; Qu, Y.; Yang, J.; Wang, Y.; Li, F.; Yu, H. Q.; Wu, Y., Identification of Fenton-like active Cu sites by heteroatom modulation of electronic density. *Proc. Natl. Acad. Sci. U S A* **2022**, 119 (8) e2119492119.

(6) Wang, J.; Li, B.; Li, Y.; Fan, X.; Zhang, F.; Zhang, G.; Peng, W., Facile Synthesis of atomic Fe-N-C materials and dual roles investigation of Fe-N_4 Sites in Fenton-like reactions. *Adv. Sci.* **2021**, 8 (22), e2101824.

(7) Pan, Y.; Chen, Y.; Wu, K.; Chen, Z.; Liu, S.; Cao, X.; Cheong, W. C.; Meng, T.; Luo, J.; Zheng, L.; Liu, C.; Wang, D.; Peng, Q.; Li, J.; Chen, C., Regulating the coordination structure of single-atom Fe-N_xC_y catalytic sites for benzene oxidation. *Nat. Commun.* **2019**, 10 (1), 4290.

(8) Mamtani, K.; Jain, D.; Zemlyanov, D.; Celik, G.; Luthman, J.; Renkes, G.; Co, A. C.; Ozkan, U. S., Probing the oxygen reduction reaction active sites over nitrogen-doped carbon nanostructures (CN_x) in acidic media using phosphate anion. *ACS Catal.* **2016**, 6 (10), 7249-7259.

(9) Cao, R.; Thapa, R.; Kim, H.; Xu, X.; Gyu Kim, M.; Li, Q.; Park, N.; Liu, M.; Cho, J., Promotion of oxygen reduction by a bio-inspired tethered iron phthalocyanine carbon nanotube-based catalyst. *Nat. Commun.* **2013**, 4, 2076.

(10) Guo, Z.; Xie, Y.; Xiao, J.; Zhao, Z. J.; Wang, Y.; Xu, Z.; Zhang, Y.; Yin, L.; Cao, H.; Gong, J., Single-atom Mn-N_4 site-catalyzed peroxone reaction for the efficient production of hydroxyl radicals in an acidic solution. *J. Am. Chem. Soc.* **2019**, 141 (30), 12005-12010.

(11) Shi, Y.; Ma, Z. R.; Xiao, Y. Y.; Yin, Y. C.; Huang, W. M.; Huang, Z. C.; Zheng, Y. Z.; Mu, F. Y.; Huang, R.; Shi, G. Y.; Sun, Y. Y.; Xia, X. H.; Chen, W., Electronic metal-support

538 interaction modulates single-atom platinum catalysis for hydrogen evolution reaction. *Nat.*
539 *Commun.* **2021**, 12 (1), 3021.
540 (12) Sun, S.; Hartono, N. T. P.; Ren, Z. D.; Oviedo, F.; Buscemi, A. M.; Layurova, M.; Chen,
541 D. X.; Ogunfunmi, T.; Thapa, J.; Ramasamy, S.; Settens, C.; DeCost, B. L.; Kusne, A. G.; Liu, Z.;
542 Tian, S. I. P.; Peters, I. M.; Correa-Baena, J.-P.; Buonassisi, T., Accelerated development of
543 perovskite-inspired materials via high-throughput synthesis and machine-learning diagnosis. *Joule*
544 **2019**, 3 (6), 1437-1451.
545 (13) Brown, K. A.; Brittman, S.; Maccaferri, N.; Jariwala, D.; Celano, U., Machine learning in
546 nanoscience: Big data at small scales. *Nano Lett.* **2020**, 20 (1), 2-10.
547 (14) Han, Y.; Tang, B.; Wang, L.; Bao, H.; Lu, Y.; Guan, C.; Zhang, L.; Le, M.; Liu, Z.; Wu,
548 M., Machine-learning-driven synthesis of carbon dots with enhanced quantum yields. *ACS Nano*
549 **2020**, 14 (11), 14761-14768.
550 (15) Moosavi, S. M.; Jablonka, K. M.; Smit, B., The role of machine learning in the
551 understanding and design of materials. *J. Am. Chem. Soc.* **2020**, 142, 20273-20287.
552 (16) Ekins, S.; Puhl, A. C.; Zorn, K. M.; Lane, T. R.; Russo, D. P.; Klein, J. J.; Hickey, A. J.;
553 Clark, A. M., Exploiting machine learning for end-to-end drug discovery and development. *Nat.*
554 *Mater.* **2019**, 18 (5), 435-441.
555 (17) Jordan, M. I.; Mitchell, T. M., Machine learning: Trends, perspectives, and prospects.
556 *Science* **2015**, 349 (6245), 255-260.
557 (18) Ghahramani, Z., Probabilistic machine learning and artificial intelligence. *Nature* **2015**,
558 521 (7553), 452-459.
559 (19) Gaultois, M. W.; Oliynyk, A. O.; Mar, A.; Sparks, T. D.; Mulholland, G. J.; Meredig, B.,
560 Perspective: Web-based machine learning models for real-time screening of thermoelectric
561 materials properties. *APL Materials* **2016**, 4 (5), 053213.
562 (20) Wei, H.; Zhao, S.; Rong, Q.; Bao, H., Predicting the effective thermal conductivities of
563 composite materials and porous media by machine learning methods. *Int. J. Heat Mass Transf.*
564 **2018**, 127, 908-916.
565 (21) Ju, S.; Shiga, T.; Feng, L.; Hou, Z.; Tsuda, K.; Shiomi, J., Designing nanostructures for
566 phonon transport via bayesian optimization. *Phys. Rev. X* **2017**, 7 (2), 021024.

(22) Sosso, G. C.; Deringer, V. L.; Elliott, S. R.; Csányi, G., Understanding the thermal properties of amorphous solids using machine-learning-based interatomic potentials. *Mol. Simul.* **2018**, 44 (11), 866-880.

(23) Mansouri Tehrani, A.; Oliynyk, A. O.; Parry, M.; Rizvi, Z.; Couper, S.; Lin, F.; Miyagi, L.; Sparks, T. D.; Brgoch, J., Machine learning directed search for ultraincompressible, superhard materials. *J. Am. Chem. Soc.* **2018**, 140 (31), 9844-9853.

(24) Chen, C.; Ye, W.; Zuo, Y.; Zheng, C.; Ong, S. P., Graph networks as a universal machine learning framework for molecules and crystals. *Chem. Mater.* **2019**, 31 (9), 3564-3572.

(25) Evans, J. D.; Coudert, F.-X., Predicting the mechanical properties of zeolite frameworks by machine learning. *Chem. Mater.* **2017**, 29 (18), 7833-7839.

(26) Rosenbrock, C. W.; Homer, E. R.; Csányi, G.; Hart, G. L. W., Discovering the building blocks of atomic systems using machine learning: application to grain boundaries. *npj Comput. Mater.* **2017**, 3 (1), 29.

(27) Ziletti, A.; Kumar, D.; Scheffler, M.; Ghiringhelli, L. M., Insightful classification of crystal structures using deep learning. *Nat. Commun.* **2018**, 9 (1), 2775.

(28) Daeyaert, F.; Ye, F.; Deem, M. W., Machine-learning approach to the design of OSDAs for zeolite beta. *Proc. Natl. Acad. Sci. U S A* **2019**, 116 (9), 3413-3418.

(29) Xu, M.; Tang, B.; Lu, Y.; Zhu, C.; Lu, Q.; Zhu, C.; Zheng, L.; Zhang, J.; Han, N.; Fang, W.; Guo, Y.; Di, J.; Song, P.; He, Y.; Kang, L.; Zhang, Z.; Zhao, W.; Guan, C.; Wang, X.; Liu, Z., Machine learning driven synthesis of few-layered WTe_2 with geometrical control. *J. Am. Chem. Soc.* **2021**, 143 (43), 18103-18113.

(30) Jiang, C.; Song, H.; Sun, G.; Chang, X.; Wu, S.; Zhen, S.; Zhao, Z. J.; Gong, J., D Data-driven interpretable descriptors for structure-activity relation of surface lattice oxygen on doped vanadium oxides. *Angew. Chem. Int. Ed. Engl.* **2022**, 61, e202206758.

(31) Liu, L.; Zhou, L.; Liu, D.; Yuan, W.; Chen, S.; Li, H.;. Bian Z. F; Wang, Z. L. Improved degradation efficiency of levofloxacin by a self-powered electrochemical system with pulsed direct-current. *ACS Nano* **2021**, 15(3), 5478-5485.

(32) Xu, X.; Zhang, Y.; Chen, Y.; Liu, C.; Wang, W.; Wang, J.; Huang, H.; Feng, J.; Li, Z.; Zou, Z., Revealing *OOH key intermediates and regulating H_2O_2 photoactivation by surface relaxation of Fenton-like catalysts. *Proc. Natl. Acad. Sci. U S A* **2022**, 119 (36), e2205562119.

(33) Li, X.; Huang, X.; Xi, S.; Miao, S.; Ding, J.; Cai, W.; Liu, S.; Yang, X.; Yang, H.; Gao, J.; Wang, J.; Huang, Y.; Zhang, T.; Liu, B., Single cobalt atoms anchored on porous N-doped graphene with dual reaction sites for efficient Fenton-like catalysis. *J. Am. Chem. Soc.* **2018**, 140 (39), 12469-12475.

(34) Zhu, R.; Zhu, Y.; Xian, H.; Yan, L.; Fu, H.; Zhu, G.; Xi, Y.; Zhu, J.; He, H., CNTs/ferrihydrite as a highly efficient heterogeneous Fenton catalyst for the degradation of bisphenol A: The important role of CNTs in accelerating Fe(III)/Fe(II) cycling. *Appl. Catal. B-Environ.* **2020**, 270, 118891.

(35) Feng, Y.; Liao, C.; Shih, K., Copper-promoted circumneutral activation of H_2O_2 by magnetic $CuFe_2O_4$ spinel nanoparticles: Mechanism, stoichiometric efficiency, and pathway of degrading sulfanilamide. *Chemosphere* **2016**, 154, 573-582.

(36) Shi, B.; Li, H.; Fu, X.; Zhao, C.; Li, M.; Liu, M.; Yan, W.; Yang, H., Fe single-atom catalyst for cost-effective yet highly efficient heterogeneous Fenton catalysis. *ACS Appl. Mater. Inter.* **2022**, 14 (48), 53767-53776.

(37) Su, L.; Wang, P.; Ma, X.; Wang, J.; Zhan, S., Regulating local electron density of iron single sites by introducing nitrogen vacancies for efficient photo-Fenton process. *Angew. Chem. Int. Ed. Engl.* **2021**, 60 (39), 21261-21266.

(38) He, D.; Niu, H.; He, S.; Mao, L.; Cai, Y.; Liang, Y., Strengthened Fenton degradation of phenol catalyzed by core/shell Fe-Pd@C nanocomposites derived from mechanochemically synthesized Fe-Metal organic frameworks. *Water Res.* **2019**, 162, 151-160.

(39) Yang, J.; Zeng, D.; Li, J.; Dong, L.; Ong, W.-J.; He, Y., A highly efficient Fenton-like catalyst based on isolated diatomic Fe-Co anchored on N-doped porous carbon. *Chem. Eng. J.* **2021**, 404, 126376.

(40) Fu, H.; Wei, J.; Chen, G.; Xu, M.; Liu, J.; Zhang, J.; Li, K.; Xu, Q.; Zou, Y.; Zhang, W.-x.; Xi, S.; Chen, X.; Li, S.; Ling, L., Axial coordination tuning Fe single-atom catalysts for boosting H_2O_2 activation. *Appl. Catal. B-Environ.* **2023**, 321, 122012.

(41) Wang, H.; Chen, T.; Chen, D.; Zou, X.; Li, M.; Huang, F.; Sun, F.; Wang, C.; Shu, D.; Liu, H., Sulfurized oolitic hematite as a heterogeneous Fenton-like catalyst for tetracycline antibiotic degradation. *Appl. Catal. B-Environ.* **2020**, 260, 118203.

(42) Sun, Z.; Wei, Y.; Cao, T.; Liu, Z.; Sui, R.; Li, X.; Pei, J.; Chen, Z.; Wang, S., Natural Keratin-based Fe-S_1N_3 single atom catalyst for insights into the coordination regulation effect of Fenton-like catalysis with high efficiency. *Nano Res.* **2023**.

(43) Fryer, D.; Strümke, I.; Nguyen, H., Shapley values for feature selection: The good, the bad, and the axioms. *IEEE Access* **2021**, 9, 144352-144360.

(44) An, S.; Zhang, G.; Wang, T.; Zhang, W.; Li, K.; Song, C.; Miller, J. T.; Miao, S.; Wang, J.; Guo, X., High-density ultra-small clusters and single-atom Fe sites embedded in graphitic carbon nitride (g-C_3N_4) for highly efficient catalytic advanced oxidation processes. *ACS Nano* **2018**, 12 (9), 9441-9450.

(45) Li, F.; Lu, Z.; Li, T.; Zhang, P.; Hu, C., Origin of the excellent activity and selectivity of a single-atom copper catalyst with unsaturated Cu-N_2 sites via peroxydisulfate activation: Cu(III) as a dominant oxidizing species. *Environ. Sci. Technol.* **2022**, 56, 8765-8775.

(46) Cao, P.; Quan, X.; Zhao, K.; Chen, S.; Yu, H.; Su, Y., High-efficiency electrocatalysis of molecular oxygen toward hydroxyl radicals enabled by an atomically dispersed iron catalyst. *Environ. Sci. Technol.* **2020**, 54 (19), 12662-12672.

(47) Yu, L.; Li, Y.; Ruan, Y., Dynamic control of sacrificial bond transformation in the Fe−N−C single-atom catalyst for molecular oxygen reduction. *Angew. Chem. Int. Ed. Engl.* **2021**, 60 (48), 25296-25301.

(48) Chen, X.; Ma, D.-D.; Chen, B.; Zhang, K.; Zou, R.; Wu, X.-T.; Zhu, Q.-L., Metal–organic framework-derived mesoporous carbon nanoframes embedded with atomically dispersed Fe–Nx active sites for efficient bifunctional oxygen and carbon dioxide electroreduction. *Appl. Catal. B-Environ.* **2020**, 267, 118720.

(49) Zitolo, A.; Goellner, V.; Armel, V.; Sougrati, M.-T.; Mineva, T.; Stievano, L.; Fonda, E.; Jaouen, F., Identification of catalytic sites for oxygen reduction in iron- and nitrogen-doped graphene materials. *Nat. Mater.* **2015**, 14 (9), 937-942.

(50) Jia, Q.; Ramaswamy, N.; Hafiz, H.; Tylus, U.; Strickland, K.; Wu, G.; Barbiellini, B.; Bansil, A.; Holby, E. F.; Zelenay, P.; Mukerjee, S., Experimental Observation of Redox-Induced Fe–N Switching Behavior as a Determinant Role for Oxygen Reduction Activity. *ACS Nano* **2015**, 9 (12), 12496-12505.

(51) Ferrandon, M.; Kropf, A. J.; Myers, D. J.; Artyushkova, K.; Kramm, U.; Bogdanoff, P.; Wu, G.; Johnston, C. M.; Zelenay, P., Multitechnique characterization of a polyaniline–iron–carbon oxygen reduction catalyst. *J. Phys. Chem. C* **2012**, 116 (30), 16001-16013.

(52) Ma, L.; Brow, R. K.; Choudhury, A., Structural study of Na_2O–FeO–Fe_2O_3–P_2O_5 glasses by Raman and Mössbauer spectroscopy. *J. Non. Cryst. Solids* **2014**, 402, 64-73.

(53) Xia, D.; Tang, X.; Dai, S.; Ge, R.; Rykov, A.; Wang, J.; Huang, T.-H.; Wang, K.-W.; Wei, Y.; Zhang, K.; Li, J.; Gan, L.; Kang, F., Ultrastable Fe–N–C fuel cell electrocatalysts by eliminating non-coordinating nitrogen and regulating coordination structures at high temperatures. *Adv. Mater.* **2023**, 35 (5), 2204474.

(54) Fu, H.; Li, M.; Xu, Q.; Chen, G.; Zou, Y.; Zhang, W.; Li, S.; Ling, L., Nitrogen doped carbon-distributed and nitrogen-stabilized ultrafine FeM (M = Pd, Pt, Au) nanoclusters for doxorubicin detoxification. *Appl. Catal. B-Environ.* **2022**, 316, 121646.